

SOLAR FLARES: 2D AVALANCHE MODELS AND DATA ASSIMILATION

ERIC BÉLANGER, ALAIN VINCENT, AND PAUL CHARBONNEAU

Département de physique, Université de Montréal

March 1, 2006

ABSTRACT

Solar flares play an important part in space meteorology because they can eject charged particles which are the source of the geomagnetic storms on Earth. These storms can interfere with the communication satellites and overload electric transformers. Several models to explain the mechanism of solar flares were suggested. Some authors Lu and Hamilton (1991); Lu et al. (1993); Charbonneau et al. (2001) have proposed the self-organized criticality (or avalanche) model where an instability related to the reconnection of the magnetic field lines is propagated. In this study, we propose to use together a 2D avalanche model with data assimilation. Data assimilation generates better forecasts by taking advantage of both the theoretical/numerical models and the observations. With the increase in computational power and the numerous satellites (SOHO, TRACE) observing the Sun with an improved spatial and temporal resolution, these methods will surely give us a better understanding of solar flares.

Subject headings: flares, data assimilation, self-organized criticality

1. INTRODUCTION

Solar flares are well studied because of a coupling between the Sun and the Earth: it's the Sun-Earth connection Lang (2001). Apart from the photons, a constant flux of charged particles such as protons and electrons are escaping from the Sun to form the solar wind Lang (2001). The solar wind pressure will be counteracted by the magnetosphere's magnetic pressure thus creating an equilibrium state where the magnetosphere is flattened toward the Sun Lang (2001). A solar flare can disrupt this equilibrium by ejecting extra particles thus compressing the magnetosphere: $\frac{d\vec{B}}{dt} \neq 0$. An electric field will be induced (Faraday's Law): $\frac{d\vec{B}}{dt} = -\nabla \times \vec{E}$. Electrical currents will start flowing in the ionosphere and ground causing intense aurora and affecting telecommunications Lang (2001).

The SOHO (*Solar & Heliospheric Observatory*) satellite, contains a dozen of instruments specializing in helioseismology, atmospheric teledetection and solar wind Domingo et al. (1995). The EIT telescope, on-board SOHO, is used with the LASCO coronagraph to take extreme UV (EUV) images of the transition zone and the internal corona. The passbands are given transitions of the following ions: Fe IX/X (171 Å), Fe XII (195 Å), Fe XV (284 Å) and He II (304 Å) Delaboudinière et al. (1995). Therefore, the EIT can be used in the study of solar structures like active regions, filaments and protuberances, coronal holes, coronal bright spots and polar plumes. Another instrument, the MDI (*Michelson Doppler Imager*), provides spatial and temporal averages of the full disk velocity for the study of helioseismology as well as several real-time magnetograms per day Domingo et al. (1995).

2. FLUX TUBE MODEL

The observation of the Sun by the TRACE (*Transition Region and Coronal Explorer*) satellite Handy et al. (1999), clearly shows magnetic loops formed by the solar magnetic field. These loops are made of flux tubes formed by the hot plasma caught between the magnetic field lines. Only the flux

tubes containing plasma recently heated until it emit in the EUV range can be seen on this figure.

In Fig. 1(a), such a magnetic loop is shown. At the surface of the photosphere, the gas pressure is greater than the magnetic pressure, $nk_B T \gg B^2/8\pi$, therefore the flux tubes' anchor points are affected by the random convective movement of the solar granules and supergranules Parker (1983); Lu et al. (1993). The flux tubes can be twisted by rotational motion and/or braided by translational motion (Fig. 1(b)). This can create tangential discontinuities where magnetic lines of different polarities are compressed against each other. If an instability threshold is reached, these magnetic lines will annihilate each other to reach a new, less energetic configuration: this is a magnetic reconnection. The magnetic reconnections release energy under the form of UV, X-ray and accelerated particles and were named "nanoflares" by Parker Parker (1983, 1988). Solar flares of all sizes are made from a number of nanoflares.

Several characteristics of solar flares behave as power laws such as the X-ray flux distribution maximum Lu et al. (1993); Dennis (1985), the released energy Charbonneau et al. (2001) and the waiting time distribution between flares Boffetta et al. (1999); Wheatland (2000); Norman et al. (2001). These numerous power laws indicate a scale invariance where all flares are governed by the same laws of physics. The energy frequency distribution:

$$f(E) = f_0 E^{-\alpha}, \quad \alpha > 0 \quad (1)$$

follows a power law in α for about 10 decades Aschwanden et al. (2000). The total energy released is:

$$E_{tot} = \int_{E_{min}}^{E_{max}} f(E) E dE \\ = f_0 \left(\frac{E^{2-\alpha}}{2-\alpha} \right) \Bigg|_{E_{min}}^{E_{max}}, \quad \alpha \neq 2 \quad (2)$$

The value of α is important in the study of coronal heating: if $\alpha > 2$ the small flares dominate the total energy output as speculated by Parker Parker (1988).

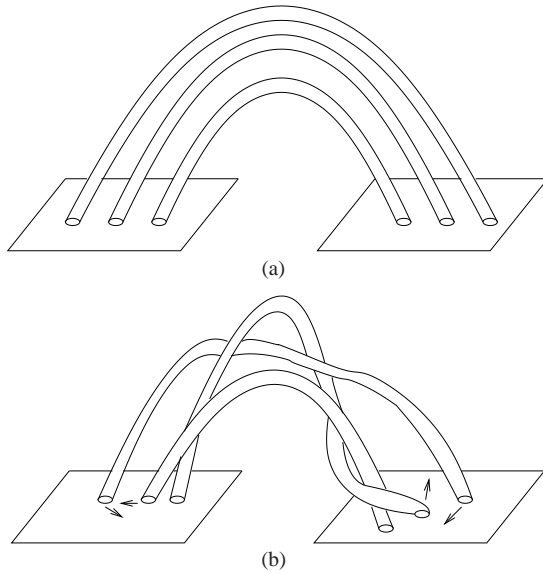


FIG. 1.— Flux tube braiding Parker (1983). The anchor point of the flux tubes (1(a)) are shuffled by the convective motion of the photosphere. Therefore, they become entangled and twisted (1(b)).

3. SELF-ORGANIZED CRITICALITY (SOC)

The numerous observed power laws suggest a scale invariance therefore solar flares might be a phenomena of self-organized criticality (SOC) Bak et al. (1987); Jensen (1998). The concept of self-organization is used in the description of non-equilibrium systems that produce structures or patterns without any external control Jensen (1998). The criticality is associated with equilibrium thermodynamics and phase change. A local perturbation will only affect the surrounding of the perturbed area unless the system is near a phase change. In this case, the perturbation will propagate throughout the whole system Jensen (1998). SOC is found in slow forcing systems with an interaction dominated threshold. The slow forcing let the system relax to a metastable state accessible through the instability threshold while preventing the dynamics to be dominated by the external forcing Jensen (1998). The advantages of the SOC models is that they require no free parameters and that they are a dynamical attractor Lu et al. (1993). An analogy can be made with a sandpile Bak et al. (1987). If the grains are dropped one by one, a conical sandpile will form. It will have a critical angle which the system will try to maintain. If we keep adding grains, they will, depending on the new slope, stay on the sandpile or cause an avalanche. Thus, the SOC models are characterized by a slow steady energy input and release it in a sudden and intermittent manner.

To apply SOC (avalanche model) to solar flares, the sandpile is replaced by a 2D lattice of metastable nodes (Fig. 2) where a scalar quantity, $A_{i,j}^n$, is defined Charbonneau et al. (2001). The lattice mean field is given by:

$$\langle A \rangle = \frac{1}{N^2} \sum_{i,j} A_{i,j}^n \quad (3)$$

(N is the lattice size) and the lattice “energy”:

$$E = \sum_{i,j} (A_{i,j}^n)^2. \quad (4)$$

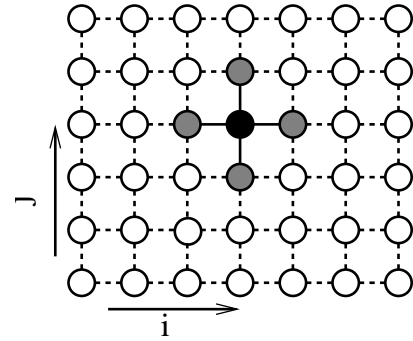


FIG. 2.— A lattice of metastable nodes where a scalar quantity A is defined. Once a perturbed node (in black) reach the instability threshold, its excess of A is redistributed among its neighbours (in grey) Charbonneau et al. (2001).

A random node is perturbed. If the local curvature of the field:

$$\Delta A_{i,j}^n \equiv A_{i,j}^n - \frac{1}{4} \sum_{\text{neighbours}} A_{\text{neighbours}}^n \quad (5)$$

gets too steep ($\Delta A_{i,j}^n > A_c$), there will be a redistribution of the quantity $A_{i,j}^n$ between the neighbouring nodes:

$$A_{i,j}^{n+1} = A_{i,j}^n - \frac{4}{5} \Delta A_{i,j}^n \quad (6)$$

and

$$A_{i\pm 1, j\pm 1}^{n+1} = A_{i\pm 1, j\pm 1}^n + \frac{1}{5} \Delta A_{i,j}^n \quad (7)$$

The excess of the quantity A will thus be diffused across the domain until stability is reached. Equations (6) and (7) can be written in a continuous form:

$$\frac{\partial A}{\partial t} = -\frac{\partial^2}{\partial x^2} \left(\nu(A_{xx}^2) \frac{\partial^2 A}{\partial x^2} \right) - \frac{\partial^2}{\partial y^2} \left(\nu(A_{yy}^2) \frac{\partial^2 A}{\partial y^2} \right) + F_R \quad (8)$$

where:

$$\nu(A_{xx}^2) = \begin{cases} \nu_a & \text{if } \Delta A^2 > A_c^2 \\ 0 & \text{else} \end{cases} \quad (9)$$

Giving a physical meaning to the scalar A is not trivial. If A is considered as being the magnetic field, then $\nabla \cdot A \neq 0$. Taking A as the vector potential, solves the non-null divergence problem. However, $\sum_{i,j} (A_{i,j}^n)^2$ lose its meaning Charbonneau et al. (2001). Here, A ($G \cdot km$) will be considered as the vector potential. The quantity ν (km^4/hr) is a viscosity term that regulates the boundary between the flaring and non-flaring regions. The forcing F_R ($(G \cdot km)/hr$) is equivalent to twisting the magnetic field locally. The parameters x and y are dimensions (km), t is time (hr), A_c is the stability threshold and ν_a is the numerical value of the viscosity ν . Equation (8) can be related to a two dimensional hyperdiffusion equation with variable viscosity. The quantity being diffused is the vector potential of the solar magnetic field.

4. DATA ASSIMILATION (4D-VAR)

So far, the separate contribution of the observational satellites and theoretical/numerical models in the comprehension of the complex phenomena of the solar flares were considered in order to make forecasts. Four-dimensional variational data assimilation (4D-VAR) is an efficient technique to incorporate observations in numerical models Courtier and Talagrand (1990); Talagrand and Courtier (1987). The 4D-VAR method consists in minimizing the cost function which is a scalar function measuring the deviation between the forecast

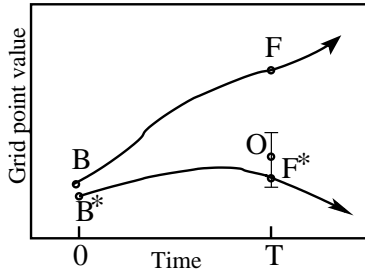


FIG. 3.— Overview of variational data assimilation. Point B is an estimate of the initial condition at time 0. Using this initial condition, a forecast F is obtained at time T . The 4D-VAR method uses the difference between the forecast F and the observation O to generate a new initial condition B^* which will produce a better forecast (F^*) at time T Errico (1997).

and the observations. The physical fields produced by data assimilation must correspond to the observations while following the known physical laws and/or statistical relations Le Dimet and Talagrand (1986).

Figure 3 shows an overview of the 4D-VAR method specifically the evolution of a grid point value, such as the magnetic field at one point, over a time interval T . Point B is an estimate of the initial condition at time 0. Using this initial condition will result in the forecast F at time T . As it can be seen, the forecast is located beyond the observation's (O) error bar. The 4D-VAR method uses the difference between the forecast F and the observation O to generate a new initial condition B^* . If B^* is used to produce a forecast F^* at time T which is closer to the observation Errico (1997). Notice that a small perturbation $\epsilon(\Delta t)$ in the initial conditions can grow exponentially:

$$\epsilon(\Delta t) \propto e^{\Lambda \Delta t} \quad (10)$$

where Λ is a Lyapunov exponent Smith et al. (1999); Smith (2001). This is a characteristic of unstable systems Lorenz (1985); Kalnay (2003). Generally, the Lyapunov exponents of a stable system are all less or equal to zero while unstable systems have at least one exponent greater than zero Kalnay (2003). However, note that Λ will vary depending on the value of Δt and it's only when $\Delta t \rightarrow \infty$ that a positive Λ demonstrate an unstable system Smith et al. (1999); Smith (2001).

4.1. The cost function

Generally, in variational problems, we want to minimize the cost function \mathcal{J} :

$$\mathcal{J} = \int_0^T \int_{\Omega} f(\Psi, \vec{x}, t) d\vec{x} dt \quad (11)$$

where $f(\Psi, \vec{x}, t)$ is a scalar function defined over a domain Ω and a time interval $[0, T]$ Sanders and Katopodes (2000). More precisely, in data assimilation:

$$\mathcal{J} = \frac{1}{2} \int_0^T \int_{\Omega} (A - A_{\text{obs}}) \mathbf{W} (A - A_{\text{obs}}) d\vec{x} dt, \quad (12)$$

where \mathbf{W} is a matrix of statistical weights, given the physical equations:

$$\mathcal{E}(\Psi, \vec{x}, t) = 0 \quad (13)$$

acting as constraints Talagrand and Courtier (1987).

4.2. The Lagrangian formulation

We want to minimize the cost function \mathcal{J} given the constraint $\mathcal{E}(\Psi, \vec{x}, t) = 0$. Since this is a problem of minimization

with constraints, a Lagrangian formulation is used:

$$\mathcal{L}(\Psi, \lambda) = \mathcal{J}(\Psi) + \int_0^T \int_{\Omega} \lambda(\vec{x}, t) \cdot \mathcal{E}(\Psi, \vec{x}, t) d\vec{x} dt \quad (14)$$

where $\lambda(\vec{x}, t)$ are the Lagrange undetermined multipliers also called adjoint variables Sanders and Katopodes (1999). The variational operator δ is then applied on the Lagrangian to find its stationary points:

$$\begin{aligned} \delta \mathcal{L} &= \vec{\nabla}_{\Psi} \mathcal{L} \cdot \delta \Psi + \vec{\nabla}_{\lambda} \mathcal{L} \cdot \delta \lambda \\ &= \frac{\partial \mathcal{L}}{\partial \Psi} \delta \Psi + \frac{\partial \mathcal{L}}{\partial \lambda} \delta \lambda \end{aligned} \quad (15)$$

For an arbitrary displacement $(\delta \Psi, \delta \lambda)$, the minimum is reached only when $\delta \mathcal{L} = 0$ Daley (1991). This indicates that the derivative of the Lagrangian with respect to each direction must be zero:

$$\frac{\partial \mathcal{L}}{\partial \lambda} = \mathcal{E}(\Psi, \vec{x}, t) = 0 \quad (16)$$

and

$$\frac{\partial \mathcal{L}}{\partial \Psi} = \text{Adj}(\lambda) + \frac{\partial \mathcal{J}}{\partial \Psi} = 0 \quad (17)$$

where $\text{Adj}(\lambda)$ represents the adjoint equations Schröter et al. (1993). This set of equations (Eqs. 16 and 17) are the Euler-Lagrange equations as noted by Le Dimet et Talagrand (1986).

For the 2D avalanche model the direct and adjoint equations are:

$$\begin{aligned} \frac{\partial A}{\partial t} &= -\frac{\partial^2}{\partial x^2} \left(\nu(A_{xx}^2) \frac{\partial^2 A}{\partial x^2} \right) - \frac{\partial^2}{\partial y^2} \left(\nu(A_{yy}^2) \frac{\partial^2 A}{\partial y^2} \right) + F_R \quad (18) \\ \frac{\partial A^*}{\partial \tau} &= -\frac{\partial^2}{\partial x^2} \left(\nu(A_{xx}^{*2}) \frac{\partial^2 A^*}{\partial x^2} \right) - \frac{\partial^2}{\partial y^2} \left(\nu(A_{yy}^{*2}) \frac{\partial^2 A^*}{\partial y^2} \right) - \frac{\partial J}{\partial A} \quad (19) \end{aligned}$$

where A^* is the adjoint variable, τ is an inverse time ($\tau = T - t$) and J is the cost function (Eq. 12). In regard to the adjoint equation the initial condition is $A^*|_{\tau=0} = 0$. The boundary conditions are:

$$\begin{aligned} A^*(0, y, \tau) &= 0 & A^*(L_x, y, \tau) &= 0 \\ A^*(x, 0, \tau) &= 0 & A^*(x, L_y, \tau) &= 0 \\ \frac{\partial A^*}{\partial x} \Big|_{x=0} &= 0 & \frac{\partial A^*}{\partial y} \Big|_{y=0} &= 0 \\ \frac{\partial^2 A^*}{\partial x^2} \Big|_{x=0} &= 0 & \frac{\partial^2 A^*}{\partial y^2} \Big|_{y=0} &= 0 \\ \frac{\partial A^*}{\partial x} \Big|_{L_x=0} &= 0 & \frac{\partial A^*}{\partial y} \Big|_{L_y=0} &= 0 \\ \frac{\partial^2 A^*}{\partial x^2} \Big|_{L_x=0} &= 0 & \frac{\partial^2 A^*}{\partial y^2} \Big|_{L_y=0} &= 0 \end{aligned} \quad (20)$$

Starting from initial conditions obtained by current experimental observations or a previous numerical simulation, a direct simulation generates a traditional (DNS) forecast (Fig. 4). After reading the observations taken at the end of the forecast period, the initial error between the forecast and the observations is calculated. This initial error will provide a first guess to a minimization algorithm, such as the steepest descent, which will minimize the cost function (Eq. 12) with the aid of its gradient (Sec. 17). When the minimum has been found, we have a new set of initial conditions. These initial conditions are optimal because a second direct simulation using them will make an optimal forecast. The final error between this forecast and the observations will be minimal.

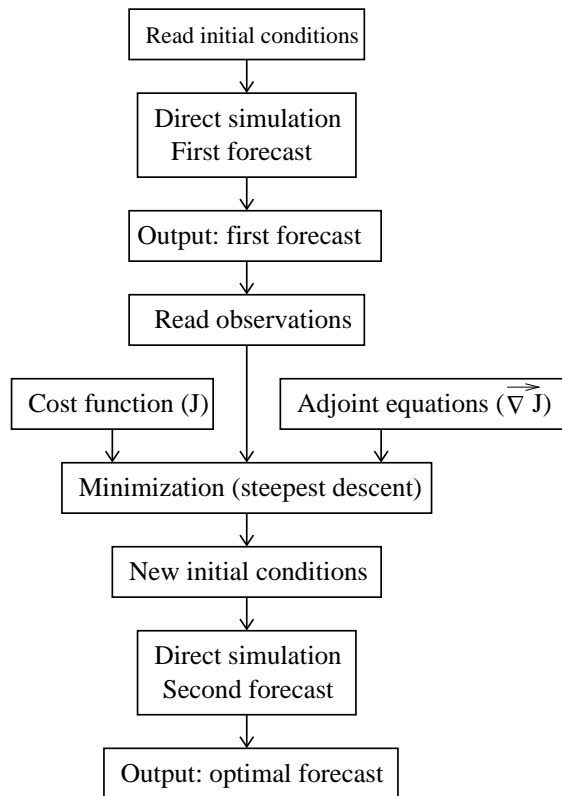


FIG. 4.— Algorithm of 4D-VAR data assimilation. From initial conditions, a traditional (DNS) forecast is made. By the use of a cost function and its gradient, the error between the forecast and the observations is minimized. A new set of initial conditions is produced. These initial conditions are optimal because a second direct simulation using them will make an optimal forecast.

5. EXPERIMENTS

We will start from a system with $A = 0$ everywhere and bring it to the SOC state. From the SOC state, we will do DNS and 4D-VAR forecast runs and compare them with the observations. This study will use synthetic observations generated from the avalanche code. The results for four runs will be presented.

Figures 6(a) and 6(b) are cross-sections along the y -axis and x -axis, respectively. They represent the evolution of the system from a null initial state (no vector potential) to the SOC regime seen as an inverse parabola. Each curve represents the vector potential at different times. Once in the SOC regime, there is no more net growth: the energy accumulated in the system is released during the avalanches. There is a clear symmetry between the x and y axis. Figure 5 shows a 3D contour plot of the domain when SOC was reached. Figure 7 represents the increase of energy ($\sum A^2$) with time. Initially, the energy gained by the system from the perturbations exceeds the energy released in avalanches. Thus, there is a net increase of the system’s energy. However, at $t \sim 3.5 \times 10^7$, a plateau is reached. The totality of the energy input is released trough avalanches: the system in in the SOC state.

Once the system has reached the SOC state, we can start making forecasts. For all runs, the cost function was minimized (Fig. 8). The non-monotonic behavior of the curves is due to the random behaviour of the avalanche model. Convergence was obtained after a few iterations. Table 1 shows the mean error in the DNS and 4D-VAR forecast of the vector potential. The 4D-VAR method has effectively reduced the mean error compared to the DNS forecasts. Hence, the

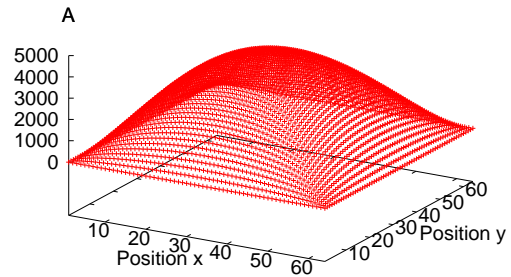


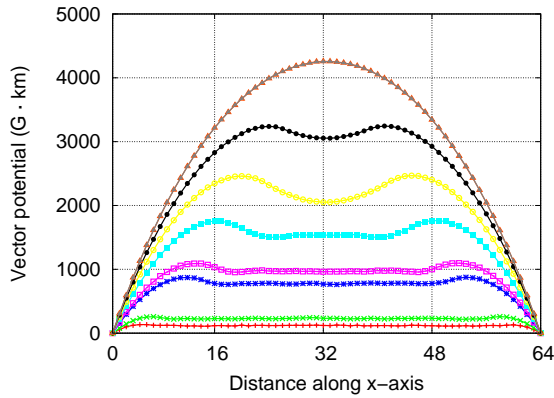
FIG. 5.— 3D contour plot of the domain.

Run	Mean DNS error ($10^{-2} G \cdot km$)	Mean 4D-VAR error ($10^{-2} G \cdot km$)
1	10.0	9.69
2	10.6	8.41
3	10.5	9.92
4	9.63	9.27

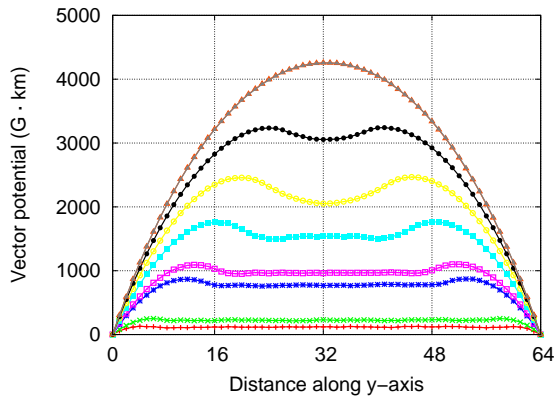
TABLE 1
DNS VERSUS 4D-VAR: MEAN ERROR IN FORECAST OF VECTOR POTENTIAL A . THE 4D-VAR FORECAST IS AN IMPROVEMENT OVER THE TRADITIONAL DNS FORECAST.

4D-VAR forecast is an improvement over the traditional DNS forecast. Furthermore, the advantage of the 4D-VAR method over DNS is also seen when the evolution over time of the total energy of the system is considered (Fig. 10). The DNS forecast (long dash) and the 4D-VAR forecast (short dash) are compared to the observation run. At the final time of 500 hours, the 4D-VAR forecast has a better correspondence to the observations than the DNS forecast. The only exception is for Run #2 where they are more or less the same. Initially, both the DNS and 4D-VAR methods matches the observations. The DNS forecast is even better than the one obtained by the 4D-VAR method. However, as time goes by the 4D-VAR forecast does a much better job at following the observations compared to the DNS forecast. The error increase between the DNS forecast and the observations can be likened to Lyapunov exponents. With the help of the cost function, the 4D-VAR method is able to undermine the error growth.

Starting from initial conditions obtained by current experimental observations or a previous numerical simulation, a direct simulation generates a traditional (DNS) forecast (Fig. 4). After reading the observations taken at the end of the forecast period, the initial error between the forecast and the observations is calculated. This initial error will provide a first guess to a minimization algorithm, such as the steepest descent, which will minimize the cost function (Eq. 12) with the aid of its gradient (Sec. 17). When the minimum has been found, we have a new set of initial conditions. These initial conditions are optimal because a second direct simulation using them will make an optimal forecast. The final error between this forecast and the observations will be minimal. An error map for both the DNS and 4D-VAR forecasts is shown in Fig. (9). These error maps, obtained with Run #2, represent the error at each grid point for the entire domain. The error is highest in avalanching (flaring) regions (cf. Fig. 11) because it is there that all the dynamic is taking place. Some regions of high error in the DNS error map (Fig. 9(a)) were completely



(a) Cross-section along the y-axis



(b) Cross-section along the x-axis

FIG. 6.— Cross-section showing the evolution of the vector potential from a null value to the SOC state (the parabolic curve). Each curve represents the vector potential at different times. The vector potential is symmetric along both axis.

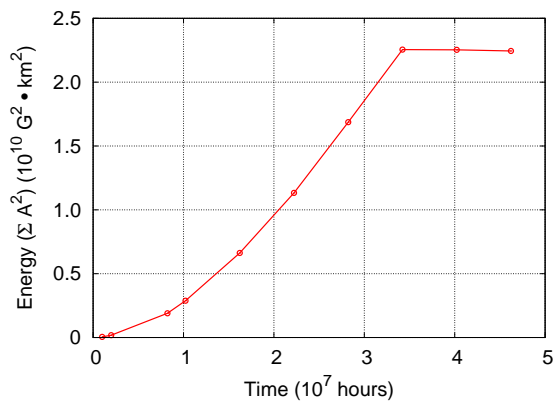


FIG. 7.— Toward the SOC state. The energy input by the perturbations is greater than the energy released in avalanches. Therefore, there is a net increase of the system’s energy. After $t \sim 3.5 \times 10^7$ hours, the SOC state is reached: the energy put in the system is released by avalanches, hence the plateau.

eliminated with the use of the 4D-VAR method (Fig. 9(b)). The small localized errors spread out through the domain are an effect of the random perturbation which will increase the potential vector at different random places. The actual forecasts are presented in Fig. 11. The DNS forecast (Fig. 11(a)) and the 4D-VAR forecast (Fig. 11(c)) are compared to the observations (Fig. 11(b)). These results were also obtained with Run #2. The forecast in the center of the large flaring

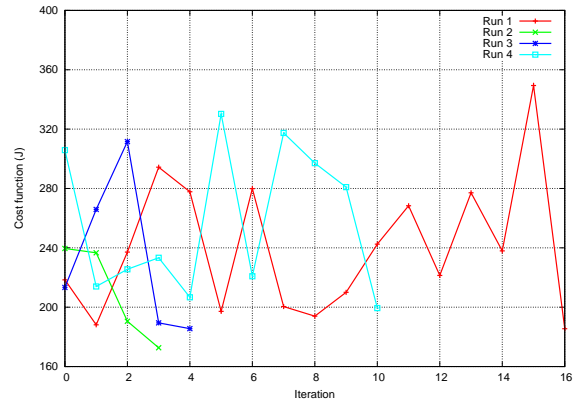


FIG. 8.— Minimization of the cost function for 4 different runs. The non-monotonic behavior is due to the randomness of the perturbations. Convergence was reached after a few iterations.

region was improved (best seen on Fig. 9) by the 4D-VAR method. It has also removed, from the DNS forecast, two small flaring regions in the upper right corner as well as another one to the right of the large flaring region. However, the 4D-VAR method was unable to remove a flaring region in the upper right corner. Also, the small flaring region near the right boundary (in Observations) is not present in the 4D-VAR forecast although the DNS forecast has a flaring region in the same vicinity. From Figure 9, it is seen that the 4D-VAR method has noticed the position offset in the DNS flaring region and has made the correction but didn’t reproduced the flaring region.

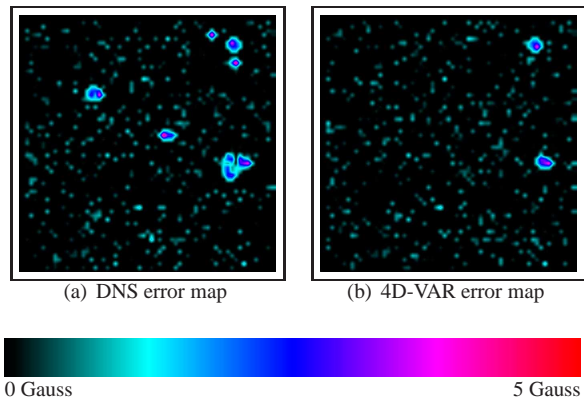


FIG. 9.— The error for each grid point over the whole domain for both the DNS (fig. 9(a)) and 4D-VAR (fig. 9(b)) forecasts. The error is highest in avalanching (flaring) regions (fig. 11). Some regions of high error were completely eliminated by the 4D-VAR method. These results were obtained with Run #2.

6. ONGOING WORK

Future work will involve using real observations from satellites (TRACE, SOHO) instead of the synthetic observations used in this study. Other work is under progress to replace the avalanche model with the full 3D MHD equations in order to compare the efficiency of data assimilation in both cases. The STEREO satellite, scheduled to launch in February 2006, will be a useful source of 3D observations. The ongoing advance in both the theoretical and observational fields will certainly provide the scientific community with a better insight about the phenomena occurring on the Sun.

REFERENCES

- Aschwanden, M. J., Tarbell, T. D., Nightingale, R. W., Schrijver, C. J., Title, A., Kankelborg, C. C., Martens, P., and Warren, H. P. (2000). Time variability of the "quiet" Sun observed with TRACE. II. Physical parameters, temperature evolution, and energetics of extreme-ultraviolet nanoflares. *Astrophysical Journal*, 535:1047–1065.
- Bak, P., Tang, C., and Wiesenfeld, K. (1987). Self-organized criticality: An explanation of $1/f$ noise. *Phys. Rev. Lett.*, 59(4):381–384.
- Boffetta, G., Carbone, V., Giuliani, P., Veltri, P., and Vulpiani, A. (1999). Power laws in solar flares: Self-organized criticality or turbulence? *Physical Review Letters*, 83:4662–4665.
- Charbonneau, P., McIntosh, S. W., Liu, H.-L., and Bogdan, T. J. (2001). Avalanche models for solar flares. *Solar Physics*, 203(2):321–353.
- Courtier, P. and Talagrand, O. (1990). Variational assimilation of meteorological observations with the direct and adjoint shallow-water equations. *Tellus*, 42A:531–549.
- Cressman, G. P. (1959). An operational objective analysis system. *Monthly Weather Review*, 87(10):367–374.
- Daley, R. (1991). *Atmospheric Data Analysis*. Cambridge atmospheric and space science series. Cambridge University Press, Cambridge.
- Delaboudinière, J.-P., Artzner, G. E., Brunaud, J., Gabriel, A. H., Hochedez, J. F., Millier, F., Song, X. Y., Au, B., Dere, K. P., Howard, R. A., Kreplin, R., Michels, D. J., Moses, J. D., Defise, J. M., Jamar, C., Rochus, P., Chauvineau, J. P., Marioge, J. P., Catura, R. C., Lemen, J. R., Shing, L., Stern, R. A., Gurman, J. B., Neupert, W. M., Maucherat, A., Clette, F., Cugnon, P., and van Dessel, E. L. (1995). EIT: Extreme-Ultraviolet Imaging Telescope for the SOHO mission. *Solar Physics*, 162:291–312.
- Dennis, B. R. (1985). Solar hard X-ray bursts. *Solar Physics*, 100:465–490.
- Domingo, V. (2002). SOHO, Yohkoh, Ulysses and Trace: The four solar missions in perspective, and available resources. *Astrophysics and Space Science*, 282:171–188.
- Domingo, V., Fleck, B., and Poland, A. I. (1995). The SOHO Mission: an Overview. *Solar Physics*, 162:1–37.
- Errico, R. M. (1997). What is an adjoint model? *Bulletin of the American Meteorological Society*, 78(11):2577–2591.
- Handy, B. N., Acton, L. W., Kankelborg, C. C., Wolfson, C. J., Akin, D. J., Bruner, M. E., Carvalho, R., Catura, R. C., Chevalier, R., Duncan, D. W., Edwards, C. G., Feinstein, C. N., Freeland, S. L., Friedlaender, F. M., Hoffmann, C. H., Hurlburt, N. E., Jurcevich, B. K., Katz, N. L., Kelly, G. A., Lemen, J. R., Levay, M., Lindgren, R. W., Mathur, D. P., Meyer, S. B., Morrison, S. J., Morrison, M. D., Nightingale, R. W., Pope, T. P., Rehse, R. A., Schrijver, C. J., Shine, R. A., Shing, L., Strong, K. T., Tarbell, T. D., Title, A. M., Torgerson, D. D., Golub, L., Bookbinder, J. A., Caldwell, D., Cheimets, P. N., Davis, W. N., Deluca, E. E., McMullen, R. A., Warren, H. P., Amato, D., Fisher, R., Maldonado, H., and Parkinson, C. (1999). The Transition Region and Coronal Explorer. *Solar Physics*, 187:229–260.
- Jensen, H. J. (1998). *Self-Organized Criticality*. Cambridge University Press, Cambridge.
- Kalnay, E. (2003). *Atmospheric modeling, data assimilation and predictability*. Cambridge University Press, Cambridge.
- Kantha, L. H. and Clayson, C. A. (2000). *Numerical Models of Oceans and Oceanic Processes*, volume 66 of *International Geophysics Series*, chapter 14. Academic Press.
- Lang, K. R. (2001). *The Cambridge Encyclopedia of the Sun*. Cambridge University Press, New York.
- Le Dimet, F.-X. and Talagrand, O. (1986). Variational algorithms for analysis and assimilation of meteorological observations: theoretical aspects. *Tellus*, 38A:97–110.
- Lorenz, E. N. (1985). The growth of errors in prediction. In Ghil, M., editor, *Turbulence and predictability in geophysical fluid dynamics and climate dynamics*, pages 243–265. Italian Physical Society, North-Holland.
- Lu, E. T. and Hamilton, R. J. (1991). Avalanches and the distribution of solar flares. *Astrophysical Journal Letters*, 380:L89–L92.
- Lu, E. T., Hamilton, R. J., McTiernan, J. M., and Bromund, K. R. (1993). Solar flares and avalanches in driven dissipative systems. *Astrophysical Journal*, 412:841–852.
- Norman, J. P., Charbonneau, P., McIntosh, S. W., and Liu, H.-L. (2001). Waiting-time distributions in lattice models of solar flares. *Astrophysical Journal*, 557:891–896.
- Parker, E. N. (1983). Magnetic neutral sheets in evolving fields. I - General theory. *Astrophysical Journal*, 264:635–641.
- Parker, E. N. (1988). Nanoflares and the solar X-ray corona. *Astrophysical Journal*, 330:474–479.
- Sanders, B. F. and Katopodes, N. D. (1999). Control of canal flow by adjoint sensitivity method. *Journal of irrigation and drainage engineering*, 125(5):287–297.
- Sanders, B. F. and Katopodes, N. D. (2000). Adjoint sensitivity analysis for shallow-water wave control. *Journal of Engineering Mechanics*, 126(9):909–919.
- Schröter, J., Seiler, U., and Wenzel, M. (1993). Variational assimilation of GEOSAT data into an eddy-resolving model of the Gulf Stream extension area. *Journal of Physical Oceanography*, 23(5):925–953.
- Smith, L. A. (2001). Disentangling uncertainty and error: On the predictability of nonlinear systems. In Mees, A., editor, *Nonlinear Dynamics and Statistics*, pages 31–64. Birkhäuser, Boston.
- Smith, L. A., Ziehmann, C., and Fraedrich, K. (1999). Uncertainty dynamics and predictability in chaotic systems. *Quart. J. Royal Meteorological Soc.*, 125:2855–2886.
- Talagrand, O. and Courtier, P. (1987). Variational assimilation of meteorological observations with the adjoint vorticity equation. I: Theory. *Q. J. R. Meteorol. Soc.*, 113:1311–1328.
- Wheatland, M. S. (2000). The origin of the solar flare waiting-time distribution. *Astrophysical Journal*, 536:L109–L112.

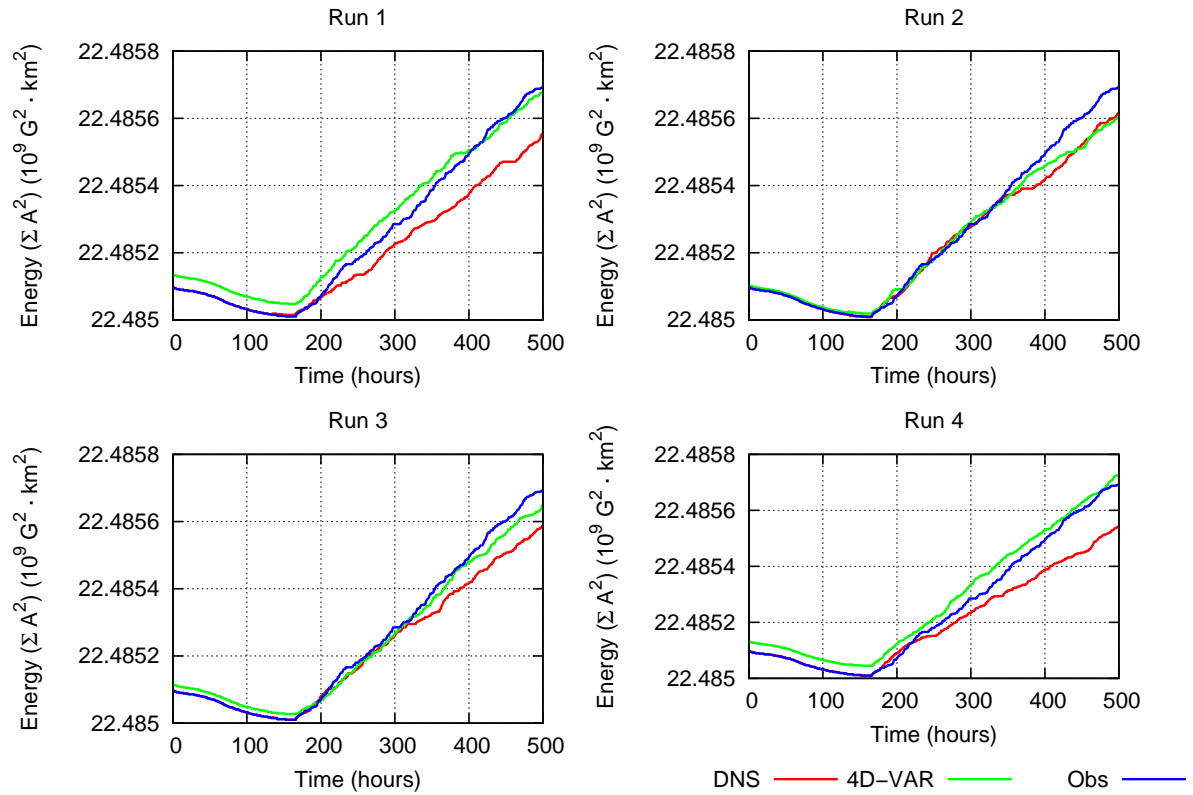


FIG. 10.— DNS & 4D-VAR: energy forecasts. At the time of 500 hours, the 4D-VAR forecast (short dash) is closer to the observations (solid) than the DNS forecast (long dash) except for Run #2 where they are more or less the same.

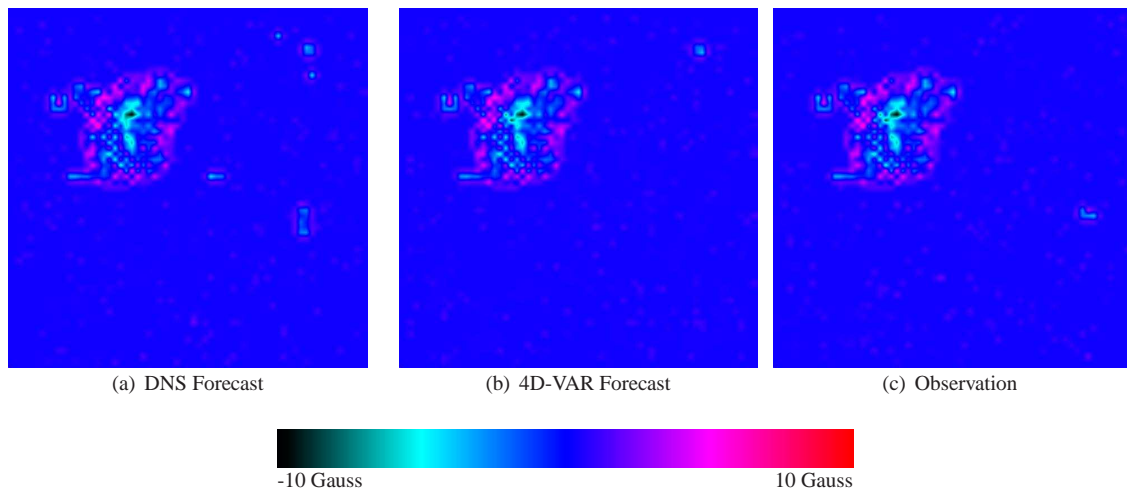


FIG. 11.— Comparison of the DNS and 4D-VAR forecasts with the observations. The 4D-VAR has slightly improved the forecast in the center of the large flaring region (barely visible on figure). It has also removed three small flaring regions (two in upper right corner and one at right of the big region). However, a circular region in upper right corner still remains and the small region near the boundary in the observation is not present. These results were obtained with Run #2.